Supplementary Material for Tunable Chiral Bound States with Giant Atoms

Xin Wang[1,2], Tao Liu[1], Anton Frisk Kockum[3], Hong-Rong Li[2] and Franco Nori[1,4]

[1] *Theoretical Quantum Physics Laboratory, RIKEN Cluster for Pioneering Research, Wako-shi, Saitama 351-0198, Japan*

[2] *MOE Key Laboratory for Nonequilibrium Synthesis and Modulation of Condensed Matter, School of Physics, Xi'an Jiaotong University, 710049, P.R.China*

[3] *Department of Microtechnology and Nanoscience, Chalmers University of Technology, 41296 Gothenburg, Sweden*

[4] *Physics Department, The University of Michigan, Ann Arbor, Michigan 48109-1040, USA*

This supplementary material includes the following: In Sec. I, we discuss the lumped-circuit model of a Josephson chain working as a metamaterial SQUID transmission line (STL), and find the parameter regime where the linear dispersion relation is valid. In Sec. II, we show how to realize a tunable photonic crystal waveguide (PCW) by periodic modulation of the STL's Josephson inductance via an external flux bias. In Sec. III, we discuss the coupling between the PCW and a superconducting giant atom, and derive the analytical form for the chiral bound states. In Sec. IV, we discuss the chiral bound state resulting from the interference effect due to nonlocal coupling of the giant atom. In Sec. V we derive, by employing standard resolvent-operator techniques, the chiral dipole-dipole interactions between giant atoms mediated by virtual photons, and discuss how to realize topological pumping of the atomic chain by shifting the modulating signal of the PCW.

CONTENTS

I. DISPERSION RELATION OF A SQUID TRANSMISSION LINE

As shown in Fig. S1(a), we consider a microwave transmission line composed of a chain of N superconducting quantum interference devices (SQUIDs), with capacitances C_g connecting each node to the ground. The SQUIDs are separated by an equal spacing d_0. The jth SQUID can be viewed as a lumped inductance L_j, in parallel with the Josephson capacitance C_j [S1–S7]. The relation between L_j and the external flux Φ_j is [S8–S10]

$$L_j = \frac{L_0}{\cos\left|\frac{\pi\Phi_j}{\Phi_0}\right|}, \quad L_0 = \frac{\Phi_0^2}{8\pi^2 E_{s0}}, \tag{S1}$$

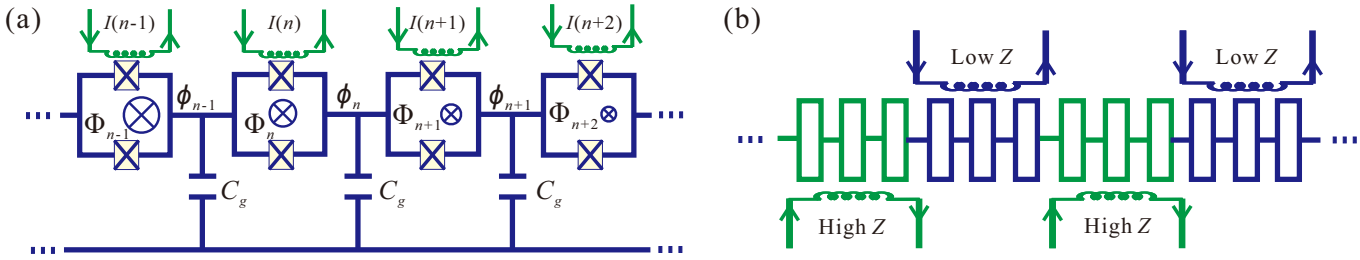

FIG. S1. (a) A SQUID-chain platform for waveguide quantum electrodynamics involving superconducting giant atoms: each SQUID works as a tunable inductance which is controlled by a bias current $I(n)$ produced by an external coil. The Josephson capacitance C_j (not shown) is in parallel with the Josephson inductance, and can be neglected in the linear-dispersion regime. At position n, the node flux is denoted by ϕ_n, with a capacitance C_g connecting to ground. (b) Instead of modulating the inductance site-by-site, the inductance of the SQUID chain (represented here by rectangles) can also be modulated group-wise. The periodic high and low impedances Z can be tuned by a common current coil, which will produce a photonic-crystal waveguide (PCW) structure.

where E_{s0} is the junction Josephson energy, which is assumed to be identical for each cite, and Φ_0 is the flux quantum. Alternatively, as indicated in Fig. S1(b), a group of SQUIDs can be tuned by sharing the same current coil. Denoting the flux at node j as ϕ_j, we obtain a Kirchoff current equation for the SQUID chain:

$$C_g\ddot{\phi}_j+\frac{\phi_j-\phi_{j-1}}{L_j}+C_j\left(\ddot{\phi}_j-\ddot{\phi}_{j-1}\right)-\frac{\phi_{j+1}-\phi_j}{L_{j+1}}-C_j\left(\ddot{\phi}_{j+1}-\ddot{\phi}_j\right)=0. \tag{S2}$$

By assuming the capacitances and effective inductances identical, $C_j=C_J$ and $L_j=L_J$, the dynamical equation in Eq. (S2) leads to the Hamiltonian [S4, S5]

$$H_0=\frac{1}{2}\vec{Q}^T\widehat{C}^{-1}\vec{Q}+\frac{1}{2}\vec{\Phi}^T\widehat{L}^{-1}\vec{\Phi}, \tag{S3}$$

$$\vec{\Phi}^T=(\phi_0,\phi_1,\ldots,\phi_N),\quad \vec{Q}=\hat{C}\dot{\vec{\Phi}}, \tag{S4}$$

where the capacitance and inductance matrices are given by

$$\widehat{C}=\begin{pmatrix} C_J & -C_J & 0 & \ldots & \\ -C_J & 2C_J+C_g & -C_J & 0 & \ldots \\ 0 & -C_J & 2C_J+C_g & -C_J & 0 \quad \ldots \\ \vdots & 0 & \ddots & \ddots & \ddots \quad \ddots \end{pmatrix}, \tag{S5}$$

and

$$\widehat{L}^{-1}=\begin{pmatrix} \frac{1}{L_J} & -\frac{1}{L_J} & 0 & \ldots & \\ -\frac{1}{L_J} & \frac{2}{L_J} & -\frac{1}{L_J} & 0 & \ldots \\ 0 & -\frac{1}{L_J} & \frac{2}{L_J} & -\frac{1}{L_J} & 0 \quad \ldots \\ \vdots & 0 & \ddots & \ddots & \ddots \quad \ddots \end{pmatrix}. \tag{S6}$$

Using the transformation $\vec{\psi}_k^s=\widehat{C}^{1/2}\vec{\Phi}$, the eigenfrequency ω_k for the system can be derived from [S4]

$$\widehat{C}^{-1/2}\widehat{L}^{-1}\widehat{C}^{-1/2}\vec{\psi}_k^s=\omega_k^2\vec{\psi}_k^s, \tag{S7}$$

where $\vec{\psi}_k^s$ is the wavefunction for mode k with frequency ω_k.

As derived in Ref. [S4], by assuming an open-ended boundary condition for the chain, the Hamiltonian in Eq. (S4) can be quantized as $H_{\rm SC}=\sum_k\hbar\omega_k(a_k^\dagger a_k+1/2)$, and the charge density operator is expressed as

$$\vec{Q}=-i\widehat{C}^{1/2}\sum_k\vec{\psi}_k^s\sqrt{\frac{\hbar\omega_k}{2}}(a_k^\dagger-a_k), \tag{S8}$$

where a_k ($a_k^\dagger$) is the annihilation (creation) operator of mode k. From Eq. (S2), we find that, due to the Josephson capacitances C_J, the equations of motion of the SQUID chain are nonlinear. In the limit $C_J \simeq 0$, the dynamical equation (S2) reduces to the lumped-element model of an ordinary 1D transmission line [S11]. In this case, the capacitance matrix is simplified to

$$\widehat{C} \simeq \mathrm{diag}[\ldots, C_g, C_g, C_g, \ldots]. \tag{S9}$$

Moreover, the eigenfunction $\vec{\psi}_k^s$ can be approximately written as

$$\vec{\psi}_k^s \simeq \sqrt{\frac{2}{N}}\left(\ldots, \sin\frac{kj\pi}{N}, \sin\frac{k(j+1)\pi}{N}, \ldots\right), \quad 0 \leqslant j \leqslant N, \tag{S10}$$

and the charge-density operator at the antinode position in Eq. (S8) is approximately expressed as

$$Q \simeq -iC_g \sum_k \sqrt{\frac{\hbar\omega_k}{C_t}}(a_k^\dagger - a_k), \tag{S11}$$

where $C_t = NC_g$ is the total capacitance of the SQUID chain. In fact, to view the whole chain as a conventional 1D SQUID transmission line (STL), the condition $C_J \simeq 0$ is too strong.

In the following, we present the parameter regime where the STL has an approximately linear dispersion relation. We use the plane-wave ansatz with $\phi = A\exp(i\omega_k t - ikjd_0)$, and by substituting it into Eq. (S2), we obtain [S3, S12]

$$\omega_k = \frac{1}{\sqrt{L_J C_g}}\sqrt{\frac{1-\cos(kd_0)}{\frac{C_J}{C_g}[1-\cos(kd_0)]+\frac{1}{2}}}. \tag{S12}$$

Moreover, we assume that the STL is approximately in the quasi-continuous regime with infinite length $L \to \infty$. Consequently, one can find that, under the conditions

$$d_0 \ll \lambda_k \ll L, \quad k \ll \frac{1}{d_0}\sqrt{\frac{C_g}{C_J}}, \tag{S13}$$

the dispersion relation is reduced to

$$\omega_{k0} \simeq \frac{kd_0}{\sqrt{L_J C_g}} = kv_J, \quad c_g = \frac{C_g}{d_0}, \quad l_J = \frac{L_J}{d_0}, \tag{S14}$$

where ω_{k0} is the mode frequency without C_J, c_g (l_J) represents the capacitance (inductance) per unit length, and $v_J = 1/\sqrt{l_J c_g}$ is the phase velocity. Under the conditions in Eq. (S14), the capacitance of Josephson junctions C_J can be neglected, and the wavefunction in Eq. (S2) is the same as that of the discretized lumped-element circuit of a 1D transmission line.

In Table I, we list the parameters employed in our numerical simulations. These parameters are adopted from the experimental work in Refs. [S3, S7, S12]. In Fig. S2(a), we plot the dispersion relation according to Eqs. (S12) and (S14), respectively. We find that, in the low-frequency regime $\omega_k/(2\pi) < 10\,\mathrm{GHz}$, the dispersion is approximately linear even with $C_J = 450C_g$. In Fig. S2(b), setting $N = 3000$, we numerically solve the eigenproblem in Eq. (S7) and plot the eigenfrequency ratio ω_k/ω_{k0} as a function of Josephson capacitance C_J and mode index k. Note that the fundamental wavevector is $k_d = 2\pi/(Nd_0)$. For nonzero C_J, the mode frequencies will be lower than those with $C_J = 0$. The parameter regime within the white curve $\omega_k/\omega_{k0} = 0.9$ is where C_J will not have significant effects. The bandwidth of the deep blue area, where the STL has linear dispersion, becomes narrower when increasing C_J/C_g and mode index (i.e., higher mode frequency). In the following discussions, we only focus on the parameters regime where the linear dispersion relation is valid.

Compared to the standard 1D transmission line, the STL has the following advantages: First, the characteristic impedance of the STL, $Z_R = \sqrt{l_J/c_g}$, can be much higher, which allows to realize strong coupling between superconducting atoms and STL modes [S7]. Second, the impedance of each SQUID in the chain is tunable via the external flux. We can thus control the impedance of the STL via local coils, and the desired dispersion relation and exotic microwave propagating effects can be conveniently tailored for quantum optics and quantum information processing. Next, in the linear dispersion regime, we propose how to realize a PCW by periodically modulating the STL's impedance.

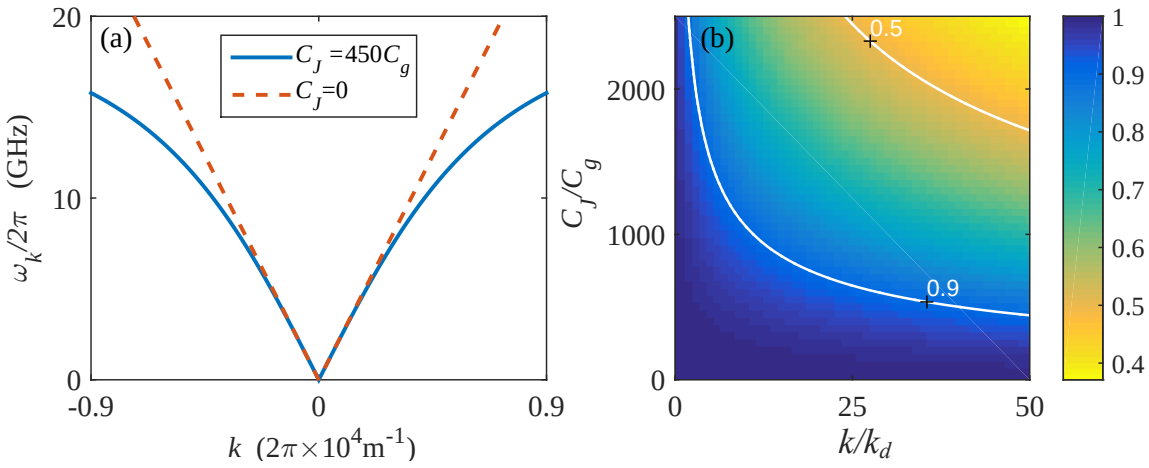

FIG. S2. (a) The dispersion relation of the SQUID chain for $C_J = 0$ and $C_J = 450C_g$, respectively. In the low-frequency limit $\omega_k < 10\,\mathrm{GHz}$, the dispersion is approximately linear. (b) The frequency ratio ω_k/ω_{k0} between $C_J = 450C_g$ and $C_J = 0$ changes with mode index k and Josephson capacitance C_J. The area delimited by the contour curve $\omega_k/\omega_{k0} = 0.9$ is the parameter regime where the linear dispersion relation is approximately valid. The considered SQUID number is $N = 3000$.

d_0	C_g	C_J	L_0	α_0	$\delta\alpha$	k_m	v_J
$1\,\mu$m	0.4 fF	90 fF	0.2 nH	0.3	0.045	$2\pi\times0.3\times10^4\,\mathrm{m}^{-1}$	$\sim10^6$ m/s

TABLE I. The lumped-circuit parameters of the microwave PCW based on a SQUID chain that we employed for numerical simulations.

II. PHOTONIC CRYSTAL WAVEGUIDES VIA SPATIALLY MODULATING THE IMPEDANCE

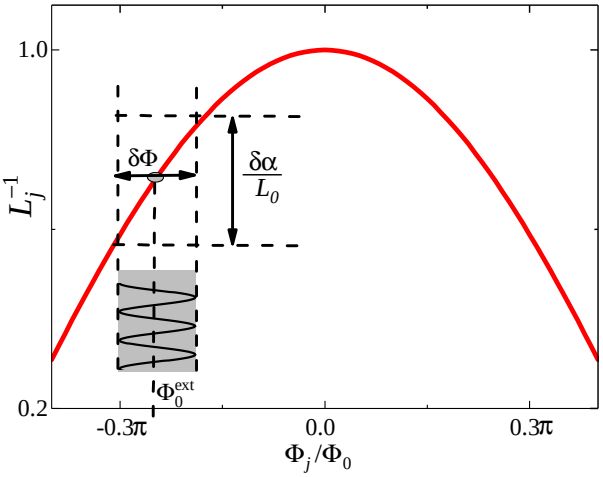

FIG. S3. The parameter L_j^{-1} changes with external flux bias around Φ_0^{ext}. The photonic crystal waveguide (PCW) is realized by periodically modulating the impedance with a bandwidth $\delta\alpha/L_0$.

As depicted in Fig. (S1), to periodically modulate the STL's impedance, we consider that the flux in each SQUID loop is independently controlled by a dc modulator according to the relation

$$\Phi_j = \Phi_0^{\mathrm{ext}} + \delta\Phi f(j), \tag{S15}$$

where Φ_0^{ext} is the static flux, $\delta\Phi$ is the modulation amplitude, and f_j is the position-dependent modulation signals. The modulation is depicted in Fig. (S3). We assume the STL is working as a microwave PCW, where the modulation is periodic in space. Then, the Josephson inductance can be written as

$$\frac{1}{L_j} \simeq \frac{1}{L_0}\left[\alpha_0 + \delta\alpha f(j)\right], \quad \alpha_0 = \cos\left(\frac{\pi\Phi_0^{\text{ext}}}{\Phi_0}\right), \tag{S16}$$

$$\delta\alpha = -\sin\left(\frac{\pi\Phi_0^{\text{ext}}}{\Phi_0}\right)\frac{\pi\delta\Phi}{\Phi_0}. \tag{S17}$$

The inductance term in Eq. (S2) is rewritten as

$$\frac{\phi_j - \phi_{j-1}}{L_j} - \frac{\phi_{j+1} - \phi_j}{L_{j+1}} = \frac{\phi_j - \phi_{j-1}}{L_j} - \frac{\phi_{j+1} - \phi_j}{L_j} + \frac{\phi_{j+1} - \phi_j}{L_j} - \frac{\phi_{j+1} - \phi_j}{L_{j+1}}. \tag{S18}$$

We assume that the distance d_0 between neighboring SQUIDs is much smaller than the wavelength of the field. Therefore, by replacing $jd_0 \to x$, we use quasi-continuous functions to describe the modulation signal and fields. Consequently, we have

$$\phi_j(t) \to \phi(x,t), \quad f(j) = f(x). \tag{S19}$$

Moreover, by defining the inductance and capacitance per unit length for the STL

$$l(x) = \frac{L_0}{d_0}\frac{1}{\alpha_0 + \delta\alpha f(x)}, \quad c_{g,J} = \frac{C_{g,J}}{d_0}, \tag{S20}$$

Eq. (S18) is rewritten as

$$\frac{\phi_j - \phi_{j-1}}{L_j} - \frac{\phi_{j+1} - \phi_j}{L_{j+1}} = -\frac{\partial}{\partial x}\left[\frac{1}{l(x)}\frac{\partial\phi(x,t)}{\partial x}\right]d_0^2. \tag{S21}$$

Similarly, the capacitance terms in Eq. (S2) can also be rewritten as a quasi-continuous function

$$C_g\ddot{\phi}_j + C_J\left(\ddot{\phi}_j - \ddot{\phi}_{j-1}\right) - C_J\left(\ddot{\phi}_{j+1} - \ddot{\phi}_j\right) = C_g\frac{\partial^2\phi(x,t)}{\partial t^2} - C_J\frac{\partial^2\phi(x,t)}{\partial t^2\partial x^2}d_0^2. \tag{S22}$$

Therefore, in the quasi-continuous regime, Eq. (S2) is written as

$$c_g\frac{\partial^2\phi(x,t)}{\partial t^2} = c_J d_0^2\frac{\partial^4\phi(x,t)}{\partial t^2\partial x^2} + \frac{\partial}{\partial x}\left[\frac{1}{l(x)}\frac{\partial\phi(x,t)}{\partial x}\right], \tag{S23}$$

where the Josephson capacitance c_J induces a nonlinear term involving both spatial and temporal differentials. For simplicity, in our numerical simulations, we first consider the modulation to be on cosine form, i.e.,

$$\frac{1}{l(x)} = \frac{d_0}{L_0}[\alpha_0 + \delta\alpha\cos(k_m x)], \tag{S24}$$

where k_m is the modulation wavevector. Consequently, the field operator $\phi(x,t)$ is written in terms of a Bloch expansion:

$$\phi(x,t) = e^{i(\omega_l t + kx)}u_k(x), \quad u_k(x) = \sum_{n=-\infty}^{n=\infty} c_{nk}e^{ink_m x}, \tag{S25}$$

where ω_l is the eigenfrequency with l the index of the energy bands, $u_k(x)$ is a spatially periodic function satisfying $u_k(x) = u_k(x + \lambda_m)$, with $\lambda_m = 2\pi/k_m$ being the period, and c_{nk} is the coefficient of the nth Fourier order for $u_k(x)$. By substituting the wave function in Eq. (S25) into Eq. (S23), we obtain the dispersion relation between $\omega_l(k)$ and k by solving the following quadratic eigenvalue problem:

$$\left[\omega_l^2(k)\hat{M}_2 + \hat{M}_0\right]\hat{U}(k) = 0, \tag{S26}$$

where

$$\hat{M}_2 = \mathrm{diag}\Big[\ldots, -c_J(d_0)^2(k+nk_m)^2 - c_g, \ldots\Big], \tag{S27}$$

$$\widehat{M}_0 = \begin{pmatrix} \ddots & \ddots & \ddots & 0 & 0 & 0 \\ \ldots & T_{n-1,n-2} & T_{n-1,n-1} & T_{n-1,n} & 0 & 0 \\ \ldots & 0 & T_{n,n-1} & T_{n,n} & T_{n,n+1} & 0 \\ \vdots & 0 & 0 & 0 & \ddots & \ddots \end{pmatrix}, \tag{S28}$$

with

$$T_{n,n} = \frac{1}{l_0}(k+nk_m)^2, \quad l_0 = \frac{L_0}{\alpha_0 d_0}, \tag{S29}$$

and

$$T_{n,n\pm1} = \frac{\delta\alpha}{2l_0}\Big\{(k+(n\pm1)k_m)^2 + (k+(n\pm1)k_m)k_m\Big\}. \tag{S30}$$

From the formulas for $\hat{M}_2$ and $T_{n,n}$, we find that, under the condition

$$c_J(d_0)^2(k+nk_m)^2 \ll c_g \quad \longrightarrow \quad k+nk_m \ll \frac{1}{d_0}\sqrt{\frac{c_g}{c_J}}, \tag{S31}$$

the nonlinear terms due to the Josephson capacitance C_J will not have significant effects. The condition in Eq. (S31) is similar to the condition for the linear dispersion in Eq. (S13). For the higher Fourier orders (large n) beyond Eq. (S31), we require that their contributions are much smaller than the lower orders. Numerical calculations indicate that by adopting small modulation amplitudes $\delta\alpha$, the coefficients c_{nk} decrease quickly with Fourier order n. Therefore, the nonlinear effects due to C_J can be neglected. In our main text, we only consider the lowest band with $l = 1$. According to Eqs. (S11) and (S25), the charge-density operator Q can be expressed with the mode operators in the first Brillouin zone (BZ)

$$Q(x) \simeq -iC_g \sum_{k\in\mathrm{BZ}} \sqrt{\frac{\hbar\omega_k}{C_t}}\Big[a_k^\dagger e^{ikx}u_k(x) - a_k e^{-ikx}u_k^*(x)\Big]. \tag{S32}$$

The above charge-density operator will be employed for the coupling between the PCW and a superconducting atom.

In Fig. S4(a), employing the parameters listed in Table. I, we plot the band structure for the Josephson-chain PCW. We find that, even under the condition $C_J = 450C_g$, the dispersion relations for the 1st and 2nd bands are well described by the linear approximation with $C_J = 0$. In the low-frequency limit, we can view the chain as a linear-dispersion medium by neglecting the Josephson capacitance under the condition in Eq. (S31). In the first Brillouin zone $k \in (-0.5k_m, 0.5k_m]$, there are two symmetric bandgaps with width Δ_g around $k = \pm 0.5k_m$, which has been predicted in studies of 1D superconducting PCWs [S13, S14]. The bandgap regime is around $\omega_k/(2\pi) \simeq 4\,\mathrm{GHz}$, which matches with the transition frequency of superconducting atoms. In Fig. S5(a), we plot the amplitudes of the Bloch wavefunctions $|u_k(x)|$ versus x for the modes around the band edge. Figure. S5(b) shows the position-dependent impedance $Z(x) = \sqrt{l(x)/c_g}$ (in units of constant impedance $Z_0 = \sqrt{l_0/c_g}$) of the PCW. We find that, for the modes in the first band, $|u_k(x)|$ are highest (lowest) at the impedance dip (peak) positions, and their spatial periods all equal λ_m.

In the following, we will discuss the waveguide QED for superconducting atoms interacting with the Josephson PCW.

III. CHIRAL BOUND STATES INDUCED BY GIANT-ATOM EFFECTS

The conventional interaction between cold atoms and a PCW requires optical trapping of each atom at a single position with the lowest (or highest) refractive index [S15, S16]. The natural atomic size is much smaller than the

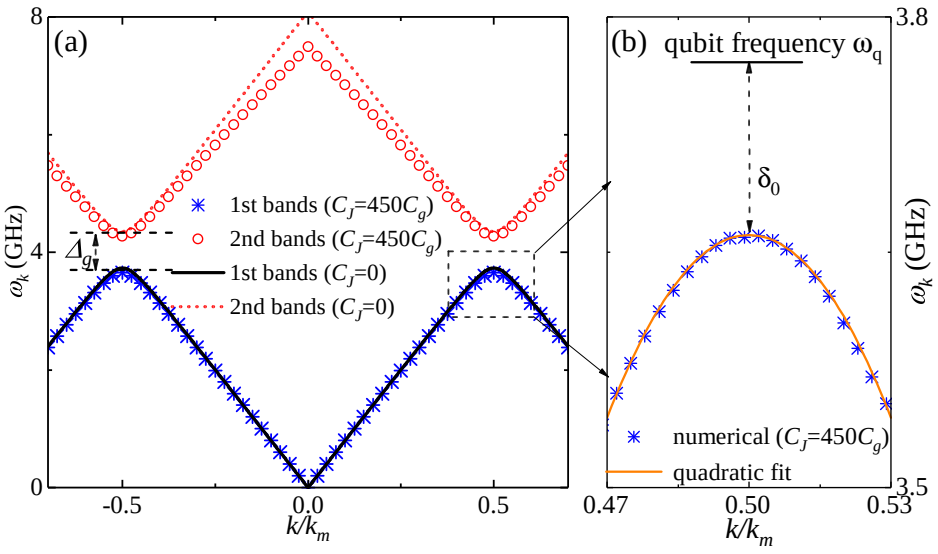

FIG. S4. (a) The two lowest bands for the PCW via spatial modulation of the SQUID inductance for $C_J = 450C_g$ and $C_J = 0$, respectively. Parameters are taken from Table I. Around $k = \pm 0.5k_m$, there are two symmetric bandgaps with width Δ_g. (b) Zoom-in around the bandgap regime. The solid curve is a quadratic fit for the dispersion relation. In our discussions, the considered atom frequency lies inside the gap with a detuning $\delta_0 = 0.1\Delta_g$.

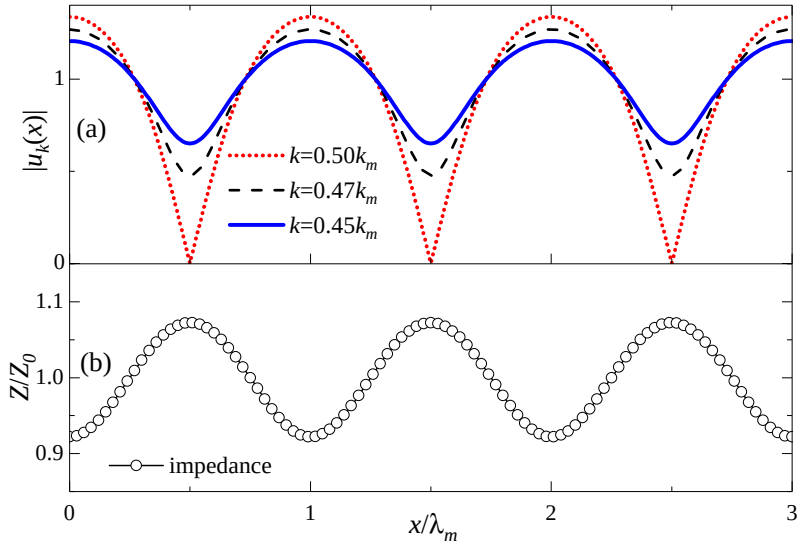

FIG. S5. (a) Amplitudes of the Bloch wavefunctions $|u_k(x)|$ as a function of x for the modes of the lowest band around the band edge. The impedance-modulating signal is depicted in (b). The PCW parameters are adopted from Table I.

length of the PCW unit cell. In solid-state SQC systems, these limitations do not exist. As shown in Fig. 1 of the main text, we consider a superconducting giant atom interacting with the PCW at two positions $x_\pm$ via capacitances $C_J^{g\pm}$. The following discussion takes the charge qubit as an example [S11], but can also be applied for the transmon qubit [S17, S18]. The Hamiltonian for the superconducting atom is expressed as

$$H_{\rm q} = 4E_C(\hat{n} - n_g)^2 - 2E_J^q \cos\left(\frac{\pi\Phi_{\rm q}}{\Phi_0}\right)\cos\phi, \tag{S33}$$

where $E_C = e^2/(2C_\Sigma)$ is the charging energy of the atom's junctions, $C_\Sigma = C_J^q + C_J^{g-} + C_J^{g+}$, with C_J^q the Josephson capacitance, and E_J^q is the Josephson energy of one junction in the atom. Note that $\Phi_{\rm q}$ is the control flux through the

split junction's loop. This flux is employed for tuning the atom's transition frequency. Around the charge degeneracy point $n_g = 1/2$, the above Hamiltonian can be quantized in a qubit basis as

$$H_{\rm q} = -E_J^q \cos\left(\frac{\pi\Phi_{\rm q}}{\Phi_0}\right)(|0\rangle\langle 1| + |1\rangle\langle 0|) - 4E_C\delta n_g(|1\rangle\langle 1| - |0\rangle\langle 0|). \tag{S34}$$

The offset-charge deviation δn_g is written as

$$\delta n_g = \sum_{\pm}\frac{Q(x_\pm)}{C_g}\frac{C_J^{g\pm}}{2e} = -i\sum_{\pm}\sum_{k\in \rm BZ}\frac{C_J^{g\pm}}{2e}\sqrt{\frac{\hbar\omega_k}{C_t}}\left[a_k^\dagger e^{ikx_\pm}u_k(x_\pm) - a_k e^{-ikx_\pm}u_k^*(x_\pm)\right], \tag{S35}$$

where $Q(x_\pm)$ is the charge-density operator at two coupling positions $x_\pm$ described by Eq, (S32). In the basis

$$|e\rangle = \frac{|1\rangle - |0\rangle}{\sqrt{2}}, \quad |g\rangle = \frac{|1\rangle + |0\rangle}{\sqrt{2}}, \tag{S36}$$

the Hamiltonian for this coupled circuit-QED system is written as

$$H_0 = \frac{1}{2}\hbar\omega_q\sigma_z + \sum_k \hbar\omega_k a_k^\dagger a_k + i\sum_k \hbar\left(g_k a_k^\dagger - g_k^* a_k\right)(\sigma_+ + \sigma_-), \tag{S37}$$

where

$$\omega_q = \frac{2E_J^q}{\hbar}\cos\left(\frac{\pi\Phi_{\rm q}}{\Phi_0}\right) \tag{S38}$$

is the atomic transition frequency. The giant-atom coupling strength with mode k is

$$g_k = \sum_{i=\pm} g_k^i e^{ikx_i}u_k(x_i), \quad g_k^\pm = \frac{e}{\hbar}\frac{C_J^{g\pm}}{C_\Sigma}\sqrt{\frac{\hbar\omega(k)}{C_t}} \simeq \frac{e}{\hbar}\frac{C_J^{g\pm}}{C_\Sigma}\sqrt{\frac{\hbar\omega_q}{C_t}}, \tag{S39}$$

where the mode frequency $\omega(k)$ is approximately replaced by the qubit frequency ω_q. Consequently, $g_k^\pm$ will approximately become independent of k. Note that Eq. (S39) is derived by assuming the impedance of the STL, $Z_J = \sqrt{L_J/C_g}$ is much smaller than the impedances of the coupling capacitance and the superconducting atom, i.e.,

$$Z_J \ll \max\{(\omega_q C_J^g)^{-1}, Z_q\}, \tag{S40}$$

where Z_q is the characteristic impedance of the atom, which can be estimated from its lumped-circuit model [S1]. In this case, we can view the STL as a low-impedance environment. However, compared with the conventional transmission line with character impedance $Z_0 \simeq 50\,\Omega$, Z_J can be much larger, and enables the realization of strong coupling between a superconducting atom and STL modes [S2, S7]. For example, employing the parameters in Table I, the estimated STL impedance is about $Z_J \simeq 550\,\Omega$. When the characteristic impedances of the superconducting atom and the STL match up with $Z_J \sim Z_q$, the system enters into the overdamped regime, with the coupling strength reaching its maximum value [S7]. Consequently, the coupling form in Eq. (S39) will be significantly modified. Therefore, to satisfy the impedance relation in Eq. (S40), the coupling capacitance should be smaller than that employed in the standard 1D transmission line, together with the atom working as a high-impedance circuit element.

As shown in Fig. S4, we assume that the qubit transition frequency ω_q is close to the first band, and the detuning δ_0 from the band edge is much smaller than the bandgap width Δ_g. Therefore we can approximately consider only the contributions of the first band. In our discussions here, we set $\delta_0 \simeq 0.1\Delta_g$. In a frame rotating with ω_q, adopting the rotating-wave approximation, the Hamiltonian in Eq. (S37) becomes (setting $\hbar = 1$)

$$H_{\rm int} = \sum_{k\in \rm BZ}\Delta_k(a_k^\dagger a_k) + \sum_{k\in \rm BZ}(g_k a_k^\dagger\sigma_- + g_k^* a_k\sigma_+), \tag{S41}$$

where $\Delta_k = \omega_k - \omega_q$ is the frequency detuning. We first define the spatial field operator expanded in terms of the Bloch wavefunctions

$$\phi^\dagger(x) = \frac{1}{\sqrt{L}}\sum_{k\in \rm BZ} a_k^\dagger e^{ikx}u_k(x), \tag{S42}$$

where $\phi^\dagger(x)$ $[\phi(x)]$ represents creating (annihilating) a photon at position x and satisfies $[\phi(x), \phi^\dagger(x')] = \delta(x-x')$. The bound state of the system is the eigenstate for $H_{\rm int}$ with eigenenergy ϵ_b, i.e., $H_{\rm int}|\psi_b\rangle = \epsilon_b|\psi_b\rangle$. In the single-excitation subspace, $|\psi_b\rangle$ is

$$|\psi_b\rangle = \cos(\theta)|e,0\rangle + \sin\theta \sum_k c_k |g,1_k\rangle, \tag{S43}$$

The solution for the bound state reads

$$c_k = \frac{g_k}{\tan\theta(\epsilon_b - \Delta_k)}, \tag{S44}$$

$$\epsilon_b = \sum_{k\in \rm BZ} \frac{|g_k|^2}{(\epsilon_b - \Delta_k)}, \tag{S45}$$

$$\tan\theta = \sum_{k\in \rm BZ} \frac{|g_k|^2}{(\epsilon_b - \Delta_k)^2}. \tag{S46}$$

We consider the conventional case where most of the energy of the excitation is localized in the atom, while the photonic modes are weakly populated [S13, S19]. In this case, $\cos(\theta) \simeq 1$ and $\epsilon_b \simeq 0$. Consequently, the wavefunction $\phi_b(x)$ of the photonic part in the PCW is

$$\begin{aligned}\phi_b(x) &= \sin\theta\langle x| \sum_{k\in \rm BZ} c_k a_k^\dagger |0\rangle \\ &= \sum_{k\in \rm BZ} \frac{c_k \sin\theta}{\sqrt{L}} \int dx' \langle x| e^{-ikx'} u_k^*(x') \phi^\dagger(x')|0\rangle.\end{aligned} \tag{S47}$$

By substituting c_k [Eq. (S44)] into Eq. (S47), we obtain

$$\phi_b(x) \simeq \frac{\sqrt{L}}{2\pi} \int_{k\in \rm BZ} \frac{g_k u_k^*(x) e^{-ikx}}{\epsilon_b - \Delta_k} dk, \tag{S48}$$

where the integration is limited to the first BZ. As shown in Fig. 2(c) in the main text, around the band edge $k_0 \simeq k_m/2$, the real part of g_k is approximately constant. However, the imaginary part is not constant, but changes with $\delta k = k - k_0$ rapidly and linearly, which is completely different from the small-atom case. Therefore, we should write

$$g_k \simeq (A + iB\delta k), \tag{S49}$$

where A is the average of the real part for g_k around k_0 and B is the slope of the imaginary part of g_k changing with k. For giant atoms, B is non-zero. Around the band edge of the PCW, we use the effective-mass approximation by expanding the dispersion relation as a parabolic function [S19, S20]. As depicted in Fig. S4(b), the dispersion relation of the PCW is well described by a quadratic function, i.e., $\Delta_k = -\delta_0 - \alpha_m(k-k_0)^2$.

Finally, we obtain

$$\phi_b(x) \simeq A_m \sum_\pm \int_{-\infty}^{\infty} d\delta k \left[\frac{C_\pm e^{-i\delta k x}}{\sqrt{2\pi}(\sqrt{\frac{\delta_0}{\alpha_m}} \mp i\delta k)} \right], \tag{S50}$$

$$A_m = \frac{\sqrt{L} u_{k0}^*(x) e^{-ik_0 x}}{2\sqrt{2\pi\alpha_m \delta_0}}, \tag{S51}$$

where A_m is the amplitude for the bound state's photonic part, and $C_\pm$ are determined by the behavior of the imaginary and real parts of g_k:

$$C_\pm = A \pm B\sqrt{\frac{\delta_0}{\alpha_m}}. \tag{S52}$$

By integrating Eq. (S50), we obtain

$$\phi_b(x) = A_m[C_-\Theta(-x) + C_+\Theta(x)]\exp\left(-\frac{|x|}{L_{\text{eff}}}\right), \tag{S53}$$

where $L_{\text{eff}} = \sqrt{\alpha_m/\delta_0}$ is the length scale determining the exponential decay of the localized bound state with distance, which is similar to previous studies [S19, S21, S22]. Moreover, during the derivation of Eq. (S53) we assume $|x_+ - x_-| < \lambda_m \ll L_{\text{eff}}$. When considering the bound-state distribution, we have $x_+ \simeq x_- = 0$. Therefore, the photonic energy localized between two coupling points can be neglected.

IV. THE INTERFERENCE MECHANISM OF THE BOUND STATES IN GIANT ATOMS

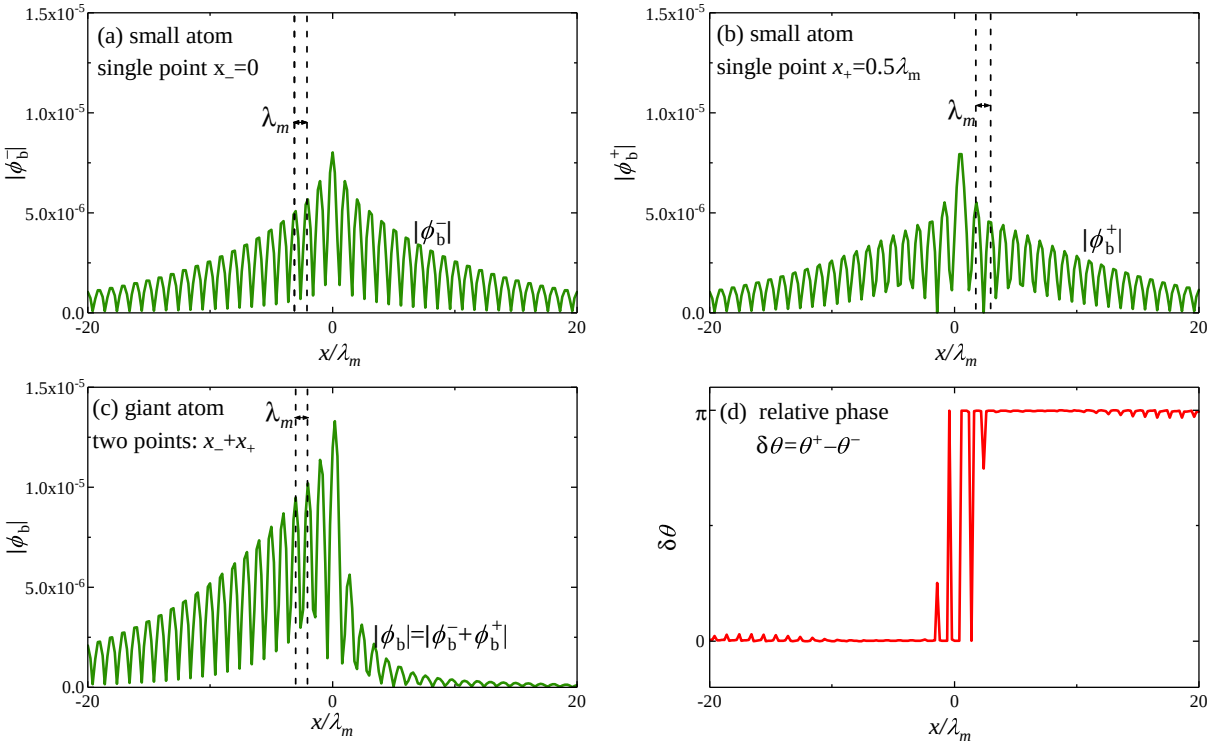

FIG. S6. By setting $\{x_-, x_+\} = \{0, 0.5\lambda_m\}$ and $g_k^+ \simeq 3.4g_k^-$, the bound-state components (a) ϕ_b^-, (b) ϕ_b^+, (c) the bound state ϕ_b, and (d) the phase difference $\delta\theta(x)$, change with position x. The PCW parameters are adopted from Fig. S4.

When considering a giant atom, the bound-state distribution in Eq. (S53) is significantly affected by the interference effects between different coupling points. To verify this, we can rewrite the bound state in Eq. (S48) as

$$\begin{gathered}\phi_b(x) = \phi_b^+(x) + \phi_b^-(x), \\ \phi_b^\pm(x) \simeq \frac{\sqrt{L}}{2\pi}\int_{k\in\text{BZ}} \frac{g_k^\pm e^{ikx_\pm}u_k(x_\pm)u_k^*(x)e^{-ikx}}{\epsilon_b - \Delta_k}dk = A_b^\pm(x)e^{i\theta_\pm(x)},\end{gathered} \tag{S54}$$

where $\phi_b^\pm(x)$ are the bound states induced by a small atom coupling at the single position $x_\pm$, and $A^\pm(x)$ $[\theta_\pm(x)]$ are their amplitudes (phases), which are both position-dependent. Equation (S54) indicates that the total bound state $\phi_b(x)$ is the result of interference effects, and is determined by the phase difference $\delta\theta(x) = \theta_+(x) - \theta_-(x)$.

In Fig. 2 of the main text, by considering x_- (x_+) at the lowest (highest) impedance position (i.e., $\{x_-, x_+\} = \{0, 0.5\lambda_m\}$), we discuss the bound-state behavior affected by the interference effects. In numerical discussions, the PCW parameters are adopted from the experimental data in Table I, and the atom frequency is assumed to be

inside the gap with a detuning $\delta_0 \simeq 0.1\Delta_g$. As depicted in Fig. S6(a, b), both $\phi_b^+(x)$ and $\phi_b^-(x)$ show no chirality. However, their phase difference is approximately described by $\delta\theta \simeq \pi\Theta(x)$, with $\Theta(x)$ the Heaviside step function [see Figure S6(d)], indicating that the interference is constructive (destructive) in the direction $x < 0$ ($x > 0$). By setting $g_k^+ \simeq 3.4g_k^-$, we find that $A^+(x) \simeq A^-(x)$. Therefore, the bound state of the giant atom is strongly localized in the left part. On the right-hand side, the bound state is mostly cancelled by the destructive interference [see Figure S6(d)]. Note that the oscillating amplitudes of the bound states are due to the periodic Bloch wavefunctions. As shown in Eq. (S48), all the periodic modes $u_k(x)$ around the band edge will contribute to the bound states $\phi_b(x)$ and $\phi_b^\pm(x)$. According to Fig. S5, $u_k(x)$ has the same period as λ_m. Therefore, the amplitude of the bound state rapidly oscillates on the scale of the decay length L_{eff}, which is much larger than the length of the PCW unit cell. For both giant and small atoms, the distance between two peaks in the bound states is also equal to λ_m (see Fig. S6).

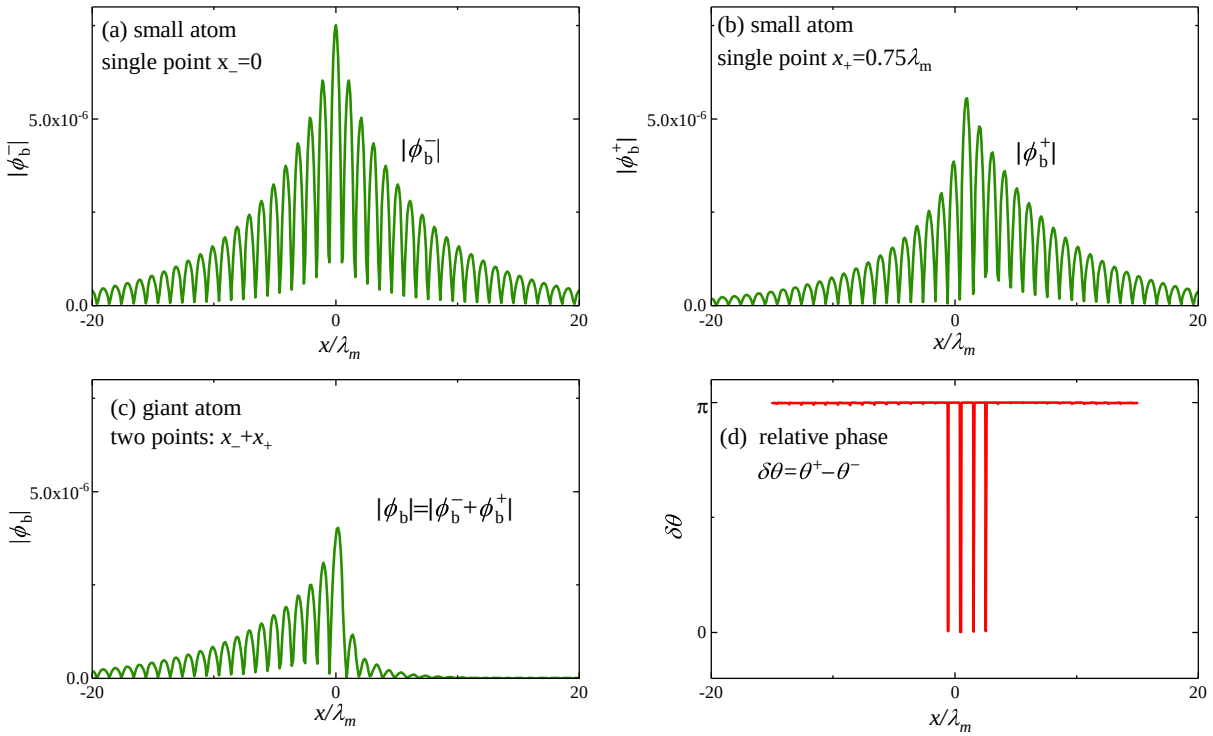

FIG. S7. By setting $\{x_-, x_+\} = \{0, 0.75\lambda_m\}$ and $g_k^- = g_k^+$, the bound-state components (a) ϕ_b^-, (b) ϕ_b^+, (c) the bound state ϕ_b, and (d) the phase difference $\delta\theta(x)$, change with the position x. The PCW parameters are adopted from Fig. S4.

When considering the second coupling point shifted to $x_+ = 0.75\lambda_m$, we find another interference pattern affecting the chirality of the bound state. In Fig. S7, we plot $\phi_b^\pm(x)$, $\phi_b(x)$ and $\delta\theta$ as a function of x. The bound state $\phi_b^+(x)$ is slightly chiral due to breaking the mirror symmetry of the PCW [see Fig. S7(b)]. However, the chirality is not large. As shown in Fig. S7(d), the phase difference $\delta\theta$ is approximately equal to π when $|x| \gg 0$. Therefore, the interference is always destructive. The amplitude for the bound state $\phi_b(x)$ of the giant atom is approximately $A_b(x) = A_b^-(x) - A_b^+(x)$. Under the condition $g_k^+ \simeq g_k^-$, we have the relations

$$\begin{aligned} A_b(x) = A_b^-(x) - A_b^+(x) \simeq 0, \qquad & x > 0, \\ A_b(-x) \gg A_b(x) \simeq 0, \qquad & x > 0, \end{aligned} \tag{S55}$$

which indicate that the bound state is strongly localized on the left side due to the quantum interference. In this case, the quantum interference effect significantly enhances the bound-state chirality.

As shown in Fig. S7, due to the destructive interference effects, the photonic energy of the bound state $\phi_b(x)$ is suppressed and smaller than $\phi_b^\pm(x)$. Similar to optical interference, we can define the interference visibility of the

bound state as

$$W = \frac{\int_{-\infty}^{\infty} dx|\phi_b(x)|^2}{\int_{-\infty}^{\infty} dx|\phi_b^+(x)|^2 + \int_{-\infty}^{\infty} dx|\phi_b^-(x)|^2}, \tag{S56}$$

from which one finds that $W = 0$ ($W = 2$) indicates that the interference is maximally destructive (constructive), and the bound state vanishes (is enhanced).

In Fig. S8(a), setting $x_- = 0$ and $g_k^- = g_k^+$, we plot the interference visibility W as a function of x_+. We find *another unconventional behaviour* of the bound state: when the separation distance satisfies

$$d_g = x_+ - x_- = (2N+1)\lambda_m$$

with N integer, $W \simeq 0$, indicating that the bound state is completely cancelled. The mechanism for the disappearance of the bound state can be understood as follows: only the modes around the band edge contribute significantly to the bound state. In the coupling formula in Eq. (S39), we approximately replace k with $k_m/2$. Therefore, for mode k, we can write

$$e^{ikx_+}u_k(x_+) = e^{ik(x_-+d_g)}u_k(x_- + d_g) \simeq \begin{cases} -e^{ikx_-}u_k(x_-), & d_g = (2N+1)\lambda_m, \\ +e^{ikx_-}u_k(x_-), & d_g = 2N\lambda_m, \end{cases} \tag{S57}$$

where we have employed the properties of the Bloch wavefunctions $u_k(x_- + N\lambda_m) = u_k(x_-)$, and $k_m\lambda_m/2 = \pi$. Equation (S57) indicates that, when $d_g = (2N+1)\lambda_m$, the interference between $\phi_b^{\pm}(x)$ will cancel the two contributions completely, leading to $\phi_b(x) \simeq 0$, i.e., the bound state vanishes completely. Conversely, at positions $d_g = 2N\lambda_m$ the interference is maximally constructive with $W \simeq 2$.

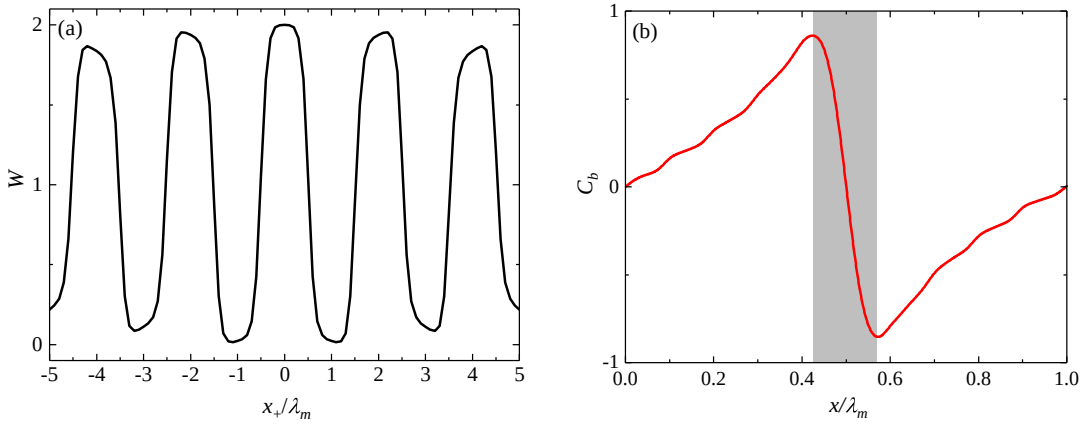

FIG. S8. (a) Setting $x_- = 0$ and $g_k^- = g_k^+$, the interference visibility W changes with the second coupling position x_+. The PCW parameters are adopted from Fig. S4. (b) The bound-state chirality changes with the coupling position of a small atom.

If a small SQC atom does not couple to the lowest (or highest) impedance position, it can see different semi-infinite waveguide structures in different directions if we split the PCW into two halves at the single coupling point. As shown in Fig. S7(b), the bound state of a small atom already shows chiral behaviour given that the coupling position is at $x_+ = 0.75\lambda_m$. In Fig. S8(b), considering a small SQC atom, we plot the chirality $\mathcal{C}_b$ [defined in Eq. (8) in the main text] as a function of the coupling position, and find that *the chirality changes rapidly* around the highest impedance position $x = 0.5\lambda_m$. The chirality for the small atom is *not* due to the quantum interference effects discussed for giant atoms. In a narrow regime $x \in [0.43\lambda_m, 0.57\lambda_m]$ (grey area), the bound state varies from close to maximally left to close to maximally right chirality, indicating that the coupling position has to be fixed accurately to achieve a certain chirality. In the giant-atom case, as depicted in Fig. 3 of the main text, the opposite chiral relations occur only when x_+ is located in the opposite direction of x_-, with a much larger separation distance. Moreover, in small-atom systems, the chirality cannot be tuned by changing the coupling strength, while in giant-atom systems, *the chirality*

can be continuously changed by modulating the relative giant-atom coupling strengths [see Fig 3(b) in the main text]. In conclusion, compared to the small atom, the chirality in giant atom system is due to a different mechanism, and is more flexible in experimental implementations.

V. CHIRAL DIPOLE-DIPOLE INTERACTIONS MEDIATED BY VIRTUAL PHOTONS

A. Chiral dipole-dipole interactions

Here we derive the chiral dipole-dipole interactions between multiple atoms induced by the giant-atom effects. We assume that all atomic transition frequencies are identical, ω_q. In a frame rotating with ω_q, the Hamiltonian of the whole system reads

$$H_0^{\mathrm{m}} = \sum_{k\in \mathrm{BZ}} \Delta_k a_k^\dagger a_k + \sum_i \sum_{k\in \mathrm{BZ}} (g_{ki}\sigma_i^- a_k^\dagger + \mathrm{H.c.}), \tag{S58}$$

where g_{ki} is given in Eq. (S39). As depicted in Fig. 4 of the main text, we first consider the intracell coupling ($i = A, B$). Since the modes $\pm k$ are degenerate with $\omega(k) = \omega(-k)$, we restrict $0 < k^+ < k_m/2$ in the positive BZ. The coupling strengths satisfy $g_{ki}^* = g_{-ki}$. The atomic operators can be written in the symmetric and antisymmetric forms as $S_\pm = (\sigma_A^- \pm \sigma_B^-)/\sqrt{2}$. Moreover, we define the supermode operator of the bath modes as

$$a_{k,\pm} = \frac{(g_{kA}^* \pm g_{kB}^*)a_k + (g_{kA} \pm g_{kB})a_{-k}}{\sqrt{2}|g_{kA} \pm g_{kB}|}, \tag{S59}$$

where the commutation relation satisfies

$$[a_{k,\beta}, a_{k',\beta'}] = \delta_{kk'}\delta_{\beta\beta'}\delta(|g_{kA}| - |g_{kB}|). \tag{S60}$$

which indicates that, under the condition $|g_{kA}| = |g_{kB}|$, the symmetric and antisymmetric operators $S_\pm$ are coupled to independent baths $a_{k,\pm}$, and their evolutions are separable [S23]. Therefore, the interaction Hamiltonian in Eq. (S58) is rewritten as

$$H_0^{\mathrm{m}} = \sum_{k^+,\beta=\pm} \Big[\Delta_k a_{k,\beta}^\dagger a_{k,\beta} + G_k^\beta (S_\beta a_{k,\beta}^\dagger + \mathrm{H.c.})\Big], \tag{S61}$$

where

$$G_k^\pm = |g_{kA} \pm g_{kB}| \tag{S62}$$

are the coupling strengths between $S_\pm$ and the supermodes $a_{k,\pm}$. Note that $\Delta_k = \omega_k - \omega_q$ in Eq. (S61) is kept unchanged but only limited by $k^+ > 0$. We denote the initial states as $|\Psi_\pm\rangle = S_\pm|g, g, 0\rangle$, where $|g(e)\rangle$ and $|0\rangle$ represent the qubit in the ground (excited) state and the PCW in the vacuum state, respectively. Using standard resolvent-operator techniques [S24], the probability amplitudes $C_\pm(t)$ ($t > 0$) that the whole system remains in $|\Psi_\pm\rangle$ are derived as

$$C_\pm(t) = \frac{i}{2\pi}\int_{-\infty}^{\infty} dE G_\pm(E + i0^+)e^{-iEt}, \tag{S63}$$

where $G_\pm(z)$ are the retarded Green functions [S24], and $z = E + i0^+$ is Fourier frequency above the real axis. Given that $|g_{kA}| = |g_{kB}|$, $G_\pm(z)$ are expressed in simple analytical forms as

$$G_\pm(z) = \frac{1}{z - \Sigma_e(z) \mp \Sigma_{AB}(z)}, \tag{S64}$$

$$\Sigma_e(z) = \int_0^{k_0} dk \frac{2(|g_{kA}|^2 + |g_{kB}|^2)}{z - \Delta_k}, \tag{S65}$$

$$\Sigma_{AB}(z) = \int_0^{k_0} dk \frac{2\Re(g_{kA}g_{kB}^*)}{z - \Delta_k}, \tag{S66}$$

where $\Sigma_e(z) \mp \Sigma_{AB}(z)$ is the atomic self-energy that describes the coupling effect between the atoms and PCW modes. In our discussions, we always assume that $|g_{kA}| \simeq |g_{kB}|$. When the coupling strengths $|g_{kA}|$ and $|g_{kB}|$ differ by a lot, the orthogonality condition of the modes $a_{k,\pm}$ in Eq. (S60) is not valid [S23]. Consequently, there is a tunnelling term $(a^\dagger_{k,+}a_{k,-} + \text{H.c.})$ between two baths, which describes the entangled evolutions between states $|\Psi_\pm\rangle$. In this case, the energy denominators for the Green functions $G_\pm(z)$ become much more complicated.

By assuming that the giant-atom couplings are sufficiently weak [S24], the standard Born-Markov approximation is valid, and we can replace E as the atom frequency. We then approximately obtain

$$\text{Re}[\Sigma_e(z)] \simeq \text{Re}[\Sigma_e(\omega_q + i0^+)] = \delta_{qs} \tag{S67}$$

$$\text{Re}[\Sigma_{AB}(z)] \simeq \text{Re}[\Sigma_{AB}(\omega_q + i0^+)] = J_{AB}, \tag{S68}$$

where the imaginary parts of $\Sigma_e(z)$ and $\Sigma_{AB}(z)$, describe the individual and collective decay of the atoms, respectively. Since the atoms interact with the PCW bandgap, in next section we show that the decay effects are strongly suppressed with a large detuning δ_0. Note that δ_{qs} represents the vacuum Stark shift of the atoms due to coupling with the PCW modes, which is the same for states $|\Psi_\pm\rangle$ [see Fig. S10(a)]. The important quantity is J_{AB}, the real part of $\Sigma_{AB}(z)$, which is in fact equal to the Rabi frequency of the coupling between states $|g, e, 0\rangle$ and $|e, g, 0\rangle$, and describes the coherent dipole-dipole coupling mediated by virtual photons in the PCW [S19, S23]. As discussed in the main text, even when the atoms are equally spaced, due to giant-atom-induced interference effects, the coupling strengths show chiral preference with $J_{AB} \neq J_{BA}$.

Finally, we discuss the effects of different kinds of impedance modulation signals on our proposal. We consider the following square and cosine modulation signals:

$$\frac{1}{l(x)} = \begin{cases} \frac{d_0}{L_0}[\alpha_0 + \delta\alpha \cos(k_m x)], & \text{cosine wave,} \\ \frac{d_0}{L_0}\{\alpha_0 + \delta\alpha \ \text{sgn}[\cos(k_m x)]\} & \text{square wave,} \end{cases} \tag{S69}$$

where sgn is the signum function. We plot the chirality $\mathcal{C}_b$ versus x_+ in Fig. S9(a). In spite of the quite different shapes of the modulation signals, their chiralities remain nearly the same. In Fig. S9(b), we show the dipole-dipole interaction strengths J_{AB} and J_{BA} as a function of the separation D_q of two atoms. Relative to the case for the cosine modulation, the coupling strengths decay a little faster for the square-wave modulation due to its smaller decay length L_{eff}. However, by comparing J_{AB} and J_{BA}, we can infer that the dipole-dipole interactions remain chiral for both impedance modulations. Therefore, our proposal is insensitive to the shape of modulation signals.

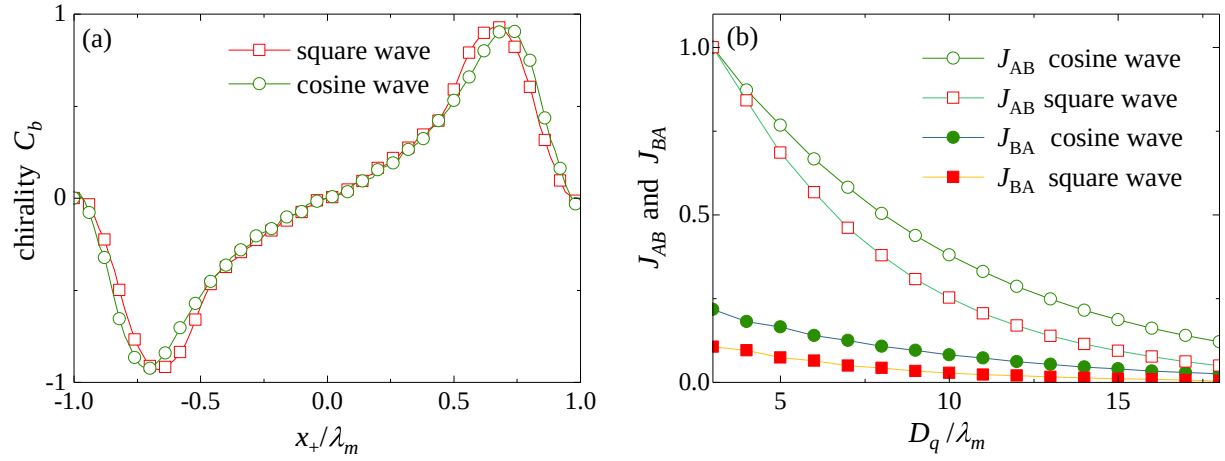

FIG. S9. (a) Chirality $\mathcal{C}_b$ as a function of x_+ for square- and cosine-wave modulations. The parameters used are the same as those in Fig. 3(a) of the main text. (b) Dipole-dipole interaction strengths J_{AB} and J_{BA} as a function of separation D_q for the two modulations. Parameters are adopted from Fig. 5(a) of the main text.

B. The decay effects of multiple atoms interacting with PCW

We now show that, with a large detuning δ_0, the atomic decay to the PCW can be effectively suppressed, and the first-order iterative results can well describe the dipole-dipole interactions between atoms. We start from Eq. (S63), which describes the probability amplitudes $C_\pm(t)$ $(t>0)$ for states $|\Psi_\pm\rangle$. It can be exactly derived via the inverse Laplace transform. To go beyond the first-order iterative approximation (i.e., assuming $z\simeq\omega_q+i0^+$), it is convenient to calculate the Laplace transform by using contour integral in the lower half-plane of the complex plane [see Fig. S10(b)]. To proceed, we need to calculate the poles of the Green function [S24, S25]

$$z-\Sigma_e(z)\mp\Sigma_{AB}(z)=0, \tag{S70}$$

which is a transcendental iterative equation, and cannot be analytically solved. As depicted in Fig. S10(a), and explained in previous section, $\Sigma_e(z)$ has the same value for both $G_\pm(z)$, which is just the Stark shift δ_{qs}. Therefore, we can simply assume $\Sigma_e(z)\simeq\delta_{qs}$ as a constant. By replacing $z-\delta_{qs}\to z$, we have

$$z\mp\Sigma_{AB}(z)=0,\quad \Sigma_{AB}(z)\simeq\frac{L}{2\pi}\int_{-k_0}^{0}d\delta k\frac{2\Re(g_{kA}g_{kB}^*)}{z+\delta_0'+\alpha_m\delta k^2}, \tag{S71}$$

where $\delta_0'=\delta_0+\delta_{qs}$ is the renormalized detuning. When the coupling g_{kA} and g_{kB} are sufficiently weak, we have $\delta_0'\simeq\delta_0$. Since only the modes around the band edge have significant contributions to the system's dynamics, the couplings can be approximate as $g_{kA}e^{-ikx_A}\simeq g_{kB}e^{-ikx_B}\simeq g_{k0}$. We note that the lower bound of the integral can be extended to $-\delta k_0\simeq-\infty$. With these approximations, $\Sigma_{AB}(z)$ can be written as

$$\Sigma_{AB}(z)\simeq\frac{\pi g_0^2}{z+\delta_0'}\frac{L}{2\pi L_{\text{eff}}}e^{-|\frac{D_q}{L_{\text{eff}}}|},\quad \sqrt{\frac{\alpha_m}{z+\delta_0'}}=L_{\text{eff}},\quad D_q=x_A-x_B, \tag{S72}$$

where $2\pi/L=dk$ is the mode discretization space of the PCW. Note that $z\mp\Sigma_{AB}(z)=0$ is still a transcendental equations. The exponential term in $\Sigma_{AB}(z)$ indicates that the qubit-qubit interactions decays as their separation distance D_q increases. This analytical result matches the numerical ones, as shown in Fig. S9(b). By taking the first-order iterative results with $z\simeq\omega_q=0$ (note that we work in the rotating frame at the atomic transition frequency), the effective decay length have the same formula in Eq. (S53).

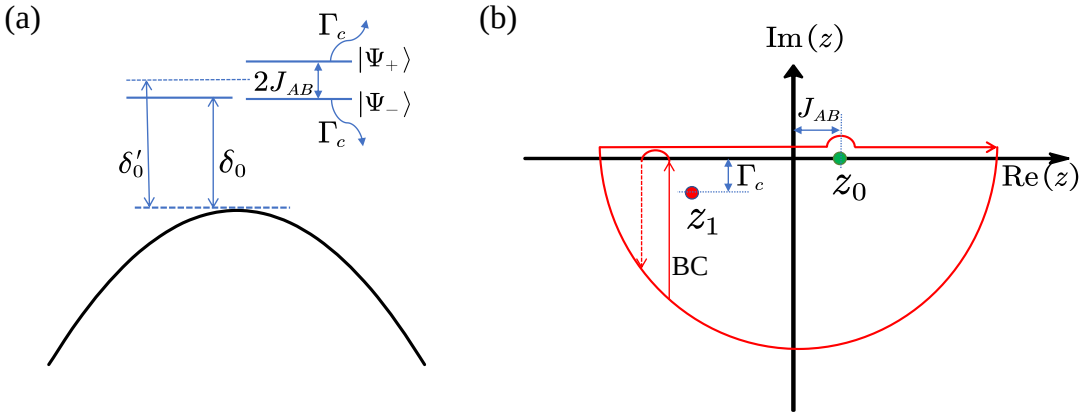

FIG. S10. (a) The energy-level diagram for two atoms interacting with the first PCW band. The detuning to the band edge of $|\Psi_\pm\rangle$ are slightly renormalized as δ_0' due to the Stark shift. The splitting between $|\Psi_+\rangle$ and $|\Psi_-\rangle$ results from the dipole-dipole interaction J_{AB}. The decay rate is denoted as Γ_c. (b) Contour integral used in the calculation $C_+(t)$. Both the inside real poles z_0 and complex poles z_1 contribute to the dynamics. The branch cut (BC) leads to apparent effects when $\delta_0'\simeq0$, which can be neglected in our discussion.

For simplicity, we consider the case where $D_q\ll L_{\text{eff}}$, i.e., the two atoms are close enough compared to the spatical

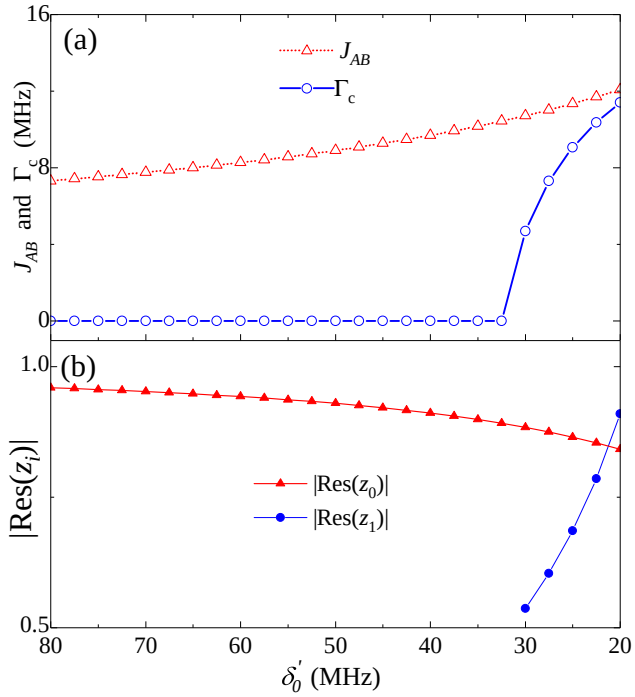

FIG. S11. (a) The dipole-dipole coupling strength J_{AB} and the atomic decay rate Γ_c versus detuning δ_0. (b) The Residues $|\mathrm{Res}(z_i)|$ of the coherent coupling and decay terms for the evolution $C_+(t)$ versus detuning δ_0'.

decay length. $\Sigma_{AB}(z)$ is now simplified as

$$\Sigma_{AB}(z) \simeq \frac{\pi g_0^2}{\sqrt{\alpha_m\left(z+\delta_0'\right)}}\frac{L}{2\pi}. \tag{S73}$$

As depicted in Fig. S10(a), the symmetric Rabi splittings between $|\Psi_\pm\rangle$ are due to the coupling between two atoms. Therefore, we can just take $|\Psi_+\rangle$ to calculate J_{AB} and the decay Γ_c. As depicted in Fig. S10(b), by solving

$$z-\Sigma_{AB}(z)=0, \tag{S74}$$

we obtain two poles for the green funtion $G_+(z)$, where z_0 (on the real axis) and z_1 (a complex pole with $\mathrm{Im}(z_1)<0$) are both inside the contour for $C_+(t)$. As discussed in Refs. [S23, S25, S26], since $\Sigma_{AB}(z)$ is a multivalued function due to the square root term $\sqrt{z+\delta_0'}$, at point $z=-\delta_0'$ one has to introduce branch cuts [BC, red dashed arrows in Fig. S10(b)]. This branch cut describes a non-exponential decay process. However, its contribution only plays an important role when the atom frequency approaches the band edge (i.e., $\delta_0'\simeq 0$) [S23]. Thus, in our discussions, we can neglect this effect. Consequently, the evolution can be derived via the residue theorem

$$C_+(t) \simeq \mathrm{Res}(z_0)e^{-iz_0t}+\mathrm{Res}(z_1)e^{-iz_1t}, \tag{S75}$$

where $\mathrm{Res}(z_i)$ are residues of the Green function $G_+(z)$

$$\mathrm{Res}(z_i)=\frac{1}{1-\partial_z\Sigma_{AB}(z)}\Big|_{z=z_i}, \quad i=0,1. \tag{S76}$$

For a small detuning δ_0', the physical processes are now clear: $|\mathrm{Im}(z_1)|=\Gamma_c$ is the atomic decay rate due to coupling to the waveguide, and z_0 just contributes to a dynamical phase due to the Rabi splitting $J_{AB}\simeq z_0$ between two atoms (without decoherence). The dynamical evolution is described as a fractional decay, where the atomic excitation is partly leaked into the PCW, and the other part is localized [S23]. The contributions of these two processes are

evaluated from their residues $|\mathrm{Res}(z_i)|$. Since the term with z_1 is unstable under decay, in the long-time limit, the probability that the atoms remain in the superposition state is [S25, S26]

$$|C(t\to\infty)|^2 \simeq |\mathrm{Res}(z_0)|^2. \tag{S77}$$

Given that $|\mathrm{Res}(z_1)| \simeq 0$ and $|\mathrm{Res}(z_0)| \simeq 1$, the atomic energy leaking into the waveguide approximately vanishes, and the interaction between two atoms is purely coherent. In this case, two atoms remain in the initial superposition state $|\Psi_+\rangle$ with $|C(t=\infty)|^2 \simeq 1$.

To evaluate J_{AB} and Γ_c, we adopt the experimentally feasible parameters listed in Table I. As depicted in Fig. S4, the PCW gap is about $\Delta_g/(2\pi) = 800$ MHz. Therefore, we set $\delta_0'/(2\pi) \sim 0.1\Delta_g = 80$ MHz in our discussion. Moreover, the coupling is set as $g_0 = 0.8$ MHz with a mode discretization space $dk = 10^{-4}k_m$. In Fig. S11(a), we plot the coupling strength $J_{AB} \simeq z_0$, and the decay rate $\Gamma_c \simeq |\mathrm{Im}(z_1)|$ versus δ_0'. Their contribution weights $|\mathrm{Res}(z_i)|$ are plotted in Fig. S11(b). We thus infer that, for a large detuning, $J_{AB} \gg \Gamma_c$ and $|\mathrm{Res}(z_0)| \simeq 1 \gg |\mathrm{Res}(z_1)|$. Note that $|\mathrm{Res}(z_0)+\mathrm{Res}(z_1)| \neq 1$ since we neglect the branch cut contribution [S23]. After $\delta_0'/(2\pi) > 30$ MHz, the complex pole z_1 disappears with $\Gamma_c = 0$ and $|\mathrm{Res}(z_0)| \simeq 1$, indicating that the coherent dipole-dipole coupling J_{AB} contributed by z_0 dominates the evolution, while the energy leaking to the PCW takes little effect. Additionally, as shown in Fig. S11(a), the dipole-dipole coupling is about $J_{AB}/(2\pi) \simeq 8$ MHz, which is strong enough in circuit-QED for quantum coherent control. Since $J_{AB} \ll \delta_0'$, it is also reasonable to adopt the first-order approximation in Eq. (S68), to calculate J_{AB} by neglecting the decay effects.

C. Topological phases with giant atoms

The chiral dipole-dipole interactions in Fig. 4 of the main text provide an ideal platform to simulate the Su-Schrieffer-Heeger (SSH model), which is described by a one-dimensional Hamiltonian with nontrivial topology [S27]. The Hamiltonian for the atomic chain reads

$$H_{\mathrm{qc}} = \sum_i (J_{AB}\sigma_{Ai}^- \sigma_{Bi}^+ + J_{BA}\sigma_{Bi}^- \sigma_{Ai+1}^+) + \mathrm{H.c.}, \tag{S78}$$

whose bulk spectrum is gapped given that $J_{AB} \neq J_{BA}$ [S28]. The relation between J_{AB} and J_{BA} determines whether the winding number is a nonzero integer or not [S29–S32]. The two lowest energy bands of H_{qc} are characterized by the topological invariant, i.e., the Zak phase $\mathcal{Z}$, and the corresponding relation is [S28]

$$J_{AB} > J_{BA}, \quad \mathcal{Z} = 0, \quad \text{trivial insulator}, \tag{S79a}$$
$$J_{AB} < J_{BA}, \quad \mathcal{Z} = \pi, \quad \text{nontrivial insulator}, \tag{S79b}$$

where the critical point $J_{AB} = J_{BA}$ corresponds to the topological phase-transition point [S32]. In the topologically nontrivial phase with $J_{AB} < J_{BA}$, there are zero-energy edge modes located at two ends of the finite chain, whose energy spectra are isolated and topologically protected from the bulk modes. In the topologically trivial phase with $J_{AB} > J_{BA}$, such edge modes do not exist. In experiments, the topological invariant is identified by the topological phase-transition process [S32–S35]. Realizing the transition between the topologically trivial and nontrivial phase of the SSH model requires tuning all coupling strengths simultaneously, as well as reversing the relation between J_{AB} and J_{BA}, which is very challenging in experiments [S31, S32].

As shown in Fig. 5(b) of the main text, such a topological transition can be easily realized by shifting the modulation signal of the PCW with a distance d_s. The impedance of the Josephson PCW is modulated via external flux signals instead of being fabricated with unchangeable parameters. Shifting the PCW modulation signal will change the interference relations and the bound-state chirality. As depicted in Fig. 4(a,b) of the main text, by shifting the programmable modulating signal a certain distance d_s, the highest-impedance positions will also be moved. The phase transition point is at $d_s = 0.25\lambda_m$, around which J_{AB} (J_{BA}) decreases (increases) linearly with d_s. By changing the flux Φ_{q} through each atom's split loop, the qubit frequency can also be modulated in time [S11].

We can map the SSH chain to the tight-binding Rice-Mele (RM) model [S33–S35]:

$$H_{\rm qc}=\sum_i\left[J_{AB}(t)\sigma_{Ai}^-\sigma_{Bi}^+ + J_{BA}(t)\sigma_{Bi}^-\sigma_{Ai+1}^+ + \text{h.c.}\right] + \sum_i \Delta_q(t)(\sigma_{Ai}^z-\sigma_{Bi}^z). \tag{S80}$$

In Fig. 6(a) of the main text, the degenerate point of the RM model is at $\{J_{BA}-J_{AB},\Delta_q\}=\{0,0\}$, which is also the phase-transition point of the SSH model. As discussed in Refs. [S33–S35], all the adiabatic quantum pump trajectories which encircle the degeneracy point are topologically equivalent, and robust to disorder and perturbations.

In our proposal, the coupling difference $J_{AB}-J_{BA}$ linearly depends on the signal shifting the distance d_s. In experiments, one can adiabatically modulate d_s back and forth in cosine form. Moreover, the qubit frequencies can be tuned in the sine form. Therefore, we can assume

$$J_{AB}(t)=1-\delta_\alpha\cos\left(\frac{2\pi t}{T}\right),\quad J_{BA}(t)=1+\delta_\alpha\cos\left(\frac{2\pi t}{T}\right),\quad \Delta_q(t)=\Omega_p\sin\left(\frac{2\pi t}{T}\right). \tag{S81}$$

As depicted in Fig. 3 in the main text, the maximum chirality of the bound state is about 0.95, indicating that J_{AB} or J_{BA} cannot be exactly zero. However, the topological pumping processes encircling the degeneracy point $\{J_{BA}-J_{AB},\Delta_q\}=\{0,0\}$ are topologically equivalent [see Fig. 6(b) in the main text], and robust to disorder and perturbations. Therefore, we just require $J_{BA}-J_{AB}$ (rather than J_{AB} and J_{BA}) to vary across zero. In Fig. 6(b) of the main text, by assuming an SSH chain with site number $N=12$, and setting the parameters as: $\delta_\alpha=0.9$, $\Omega_p=0.3$, and $T=100$, we plot the evolution of an initial excitation localized at the first site on the left edge. The minimum values for J_{AB} and J_{BA} are nonzero and equal to 0.1. As depicted in Fig. 6(b), the excitation is transferred to the right edge state at the end of each pump circle (without being disturbed by a nonzero coupling strength), and this adiabatic process is topologically protected.

[S1] N. A. Masluk, I. M. Pop, A. Kamal, Z. K. Minev, and M. H. Devoret, "Microwave characterization of Josephson junction arrays: Implementing a low loss superinductance," Phys. Rev. Lett. **109**, 137002 (2012).

[S2] C. Altimiras, O. Parlavecchio, P. Joyez, D. Vion, P. Roche, D. Esteve, and F. Portier, "Tunable microwave impedance matching to a high impedance source using a Josephson metamaterial," Appl. Phys. Lett. **103**, 212601 (2013).

[S3] T. Weissl, *Quantum phase and charge in Josephson junction chains*, Ph.D. thesis, Grenoble (2014).

[S4] T. Weißl, B. Küng, E. Dumur, A. K. Feofanov, I. Matei, C. Naud, O. Buisson, F. W. J. Hekking, and W. Guichard, "Kerr coefficients of plasma resonances in Josephson junction chains," Phys. Rev. B **92**, 104508 (2015).

[S5] M. Mirhosseini, E. Kim, V. S. Ferreira, M. Kalaee, A. Sipahigil, A. J. Keller, and O. Painter, "Superconducting metamaterials for waveguide quantum electrodynamics," Nat. Commun. **9**, 3706 (2018).

[S6] S. Karkar, E. D. Bono, M. Collet, G. Matten, M. Ouisse, and E. Rivet, "Broadband Nonreciprocal Acoustic Propagation Using Programmable Boundary Conditions: From Analytical Modeling to Experimental Implementation," Phys. Rev. Appl. **12**, 054033 (2019).

[S7] J. P. Martínez, S. Léger, N. Gheeraert, R. Dassonneville, L. Planat, F. Foroughi, Y. Krupko, O. Buisson, C. Naud, W. Hasch-Guichard, S. Florens, I. Snyman, and N. Roch, "A tunable Josephson platform to explore many-body quantum optics in circuit-QED," npj Quantum Inf. **5**, 19 (2019).

[S8] J. R. Johansson, G. Johansson, C. M. Wilson, and F. Nori, "Dynamical Casimir Effect in a Superconducting Coplanar Waveguide," Phys. Rev. Lett. **103**, 147003 (2009).

[S9] S. Pogorzalek, K. G. Fedorov, L. Zhong, J. Goetz, F. Wulschner, M. Fischer, P. Eder, E. Xie, K. Inomata, T. Yamamoto, Y. Nakamura, A. Marx, F. Deppe, and R. Gross, "Hysteretic Flux Response and Nondegenerate Gain of Flux-Driven Josephson Parametric Amplifiers," Phys. Rev. Applied **8**, 024012 (2017).

[S10] X. Wang, A. Miranowicz, and F. Nori, "Ideal Quantum Nondemolition Readout of a Flux Qubit without Purcell Limitations," Phys. Rev. Applied **12**, 064037 (2019).

[S11] X. Gu, A. F. Kockum, A. Miranowicz, Y.-X. Liu, and F. Nori, "Microwave photonics with superconducting quantum circuits," Phys. Rep. **718-719**, 1 (2017).

[S12] Y. Krupko, V. D. Nguyen, T. Weißl, É. Dumur, J. Puertas, R. Dassonneville, C. Naud, F. W. J. Hekking, D. M. Basko, O. Buisson, N. Roch, and W. Hasch-Guichard, "Kerr nonlinearity in a superconducting Josephson metamaterial," Phys. Rev. B **98**, 094516 (2018).

[S13] Y. B. Liu and A. A. Houck, "Quantum electrodynamics near a photonic bandgap," Nat. Phys. **13**, 48 (2017).

[S14] N. M. Sundaresan, R. Lundgren, G.-Y. Zhu, A. V. Gorshkov, and A. A. Houck, "Interacting Qubit-Photon Bound States with Superconducting Circuits," Phys. Rev. X **9**, 011021 (2019).

[S15] C.-L. Hung, S. M. Meenehan, D. E. Chang, O. Painter, and H. J. Kimble, "Trapped atoms in one-dimensional photonic crystals," New J. Phys. **15**, 083026 (2013).

[S16] D. E. Chang, J. S. Douglas, A. González-Tudela, C.-L. Hung, and H. J. Kimble, "Colloquium: Quantum matter built from nanoscopic lattices of atoms and photons," Rev. Mod. Phys. **90**, 031002 (2018).

[S17] J. Koch, T. M. Yu, J. Gambetta, A. A. Houck, D. I. Schuster, J. Majer, A. Blais, M. H. Devoret, S. M. Girvin, and R. J. Schoelkopf, "Charge-insensitive qubit design derived from the Cooper pair box," Phys. Rev. A **76**, 042319 (2007).

[S18] J. Q. You, X. Hu, S. Ashhab, and F. Nori, "Low-decoherence flux qubit," Phys. Rev. B **75**, 140515 (2007).

[S19] J. S. Douglas, H. Habibian, C.-L. Hung, A. V. Gorshkov, H. J. Kimble, and D. E. Chang, "Quantum many-body models with cold atoms coupled to photonic crystals," Nat. Photon. **9**, 326 (2015).

[S20] A. González-Tudela, C.-L. Hung, D. E. Chang, J. I. Cirac, and H. J. Kimble, "Subwavelength vacuum lattices and atom–atom interactions in two-dimensional photonic crystals," Nat. Photon. **9**, 320 (2015).

[S21] J. D. Hood, A. Goban, A. Asenjo-Garcia, M. Lu, S.-P. Yu, D. E. Chang, and H. J. Kimble, "Atom–atom interactions around the band edge of a photonic crystal waveguide," PNAS **113**, 10507 (2016).

[S22] J. S. Douglas, T. Caneva, and D. E. Chang, "Photon Molecules in Atomic Gases Trapped Near Photonic Crystal Waveguides," Phys. Rev. X **6**, 031017 (2016).

[S23] A. González-Tudela and J. I. Cirac, "Markovian and non-Markovian dynamics of quantum emitters coupled to two-dimensional structured reservoirs," Phys. Rev. A **96**, 043811 (2017).

[S24] C. Cohen-Tannoudji, J. Dupont-Roc, and G. Grynberg, *Atom–Photon Interactions* (Wiley, 1998).

[S25] M. Bello, G. Platero, J. I. Cirac, and A. González-Tudela, "Unconventional quantum optics in topological waveguide QED," Sci. Adv. **5**, eaaw0297 (2019).

[S26] T. Ramos, B. Vermersch, P. Hauke, H. Pichler, and P. Zoller, "Non-Markovian dynamics in chiral quantum networks with spins and photons," Phys. Rev. A **93**, 062104 (2016).

[S27] W. P. Su, J. R. Schrieffer, and A. J. Heeger, "Solitons in Polyacetylene," Phys. Rev. Lett. **42**, 1698 (1979).

[S28] T. Ozawa, H. M. Price, A. Amo, N. Goldman, M. Hafezi, L. Lu, M. C. Rechtsman, D. Schuster, J. Simon, O. Zilberberg, and I. Carusotto, "Topological photonics," Rev. Mod. Phys. **91**, 015006 (2019).

[S29] S. Ryu, A. P. Schnyder, A. Furusaki, and A. W. W. Ludwig, "Topological insulators and superconductors: tenfold way and dimensional hierarchy," New J. Phys. **12**, 065010 (2010).

[S30] C. L. Kane and T. C. Lubensky, "Topological boundary modes in isostatic lattices," Nat. Phys. **10**, 39 (2013).

[S31] M. Xiao, Z. Zhang, and C. Chan, "Surface Impedance and Bulk Band Geometric Phases in One-Dimensional Systems," Phys. Rev. X **4**, 021017 (2014).

[S32] E. S. G. Naz, I. C. Fulga, L.-B. Ma, O. G. Schmidt, and J. van den Brink, "Topological phase transition in a stretchable photonic crystal," Phys. Rev. A **98**, 033830 (2018).

[S33] M. Lohse, C. Schweizer, O. Zilberberg, M. Aidelsburger, and I. Bloch, "A Thouless quantum pump with ultracold bosonic atoms in an optical superlattice," Nat. Phys. **12**, 350 (2015).

[S34] X. Gu, S. Chen, and Y.-X. Liu, "Topological edge states and pumping in a chain of coupled superconducting qubits," (2017), arXiv:1711.06829.

[S35] S. Nakajima, T. Tomita, S. Taie, T. Ichinose, H. Ozawa, L. Wang, M. Troyer, and Y. Takahashi, "Topological Thouless pumping of ultracold fermions," Nat. Phys. **12**, 296 (2016).